

# Temperature prediction in polymer gears: semianalytical modeling

10

Carlos M.C.G. Fernandes

Faculdade de Engenharia, Universidade do Porto, Porto, Portugal

## 10.1 Polymer gear failures and the importance of bulk temperature

After conducting extensive testing on polymer gears, Hachmann and Strickle (1966) identified different types of failure. The most prevalent among them were tooth root fracture, tooth wear, tooth fracture on the pitch line, and pitting damage under lubricated conditions, which are represented in Fig. 10.1 (Walton & Shi, 1989). Later on, the VDI 2736 design guideline identified melting and permanent deformation as potential causes of polymer gear failure (VDI-2736, 2014).

Within the failures illustrated in Fig. 10.1, pitch line fracture emerges as a distinct failure mode specific to polymer gears. It predominantly occurs under dry run conditions (Hachmann & Strickle, 1966; Hall & Alvord, 1956; Terashima et al., 1986; Tsukamoto & Terashima, 1985), where the heightened coefficient of friction brings the maximum equivalent contact stress perilously close to the gear surface. This, combined with the diminished strength resulting from elevated local temperatures, initiates this particular failure. Fig. 10.1C, using blue and red colors for low and high stress, respectively, graphically portrays the distribution of equivalent contact stresses in a dry-run polymer gear with a high coefficient of friction, further emphasizing the proximity of the maximum equivalent stress to the surface. Furthermore, substantial tooth deformation under load often results in premature contact, leading to pronounced corner contact conditions between the tooth tip and the pinion tooth near its pitch point, a factor that has been associated with the potential cause of this type of failure and increased tooth wear (Karimpour et al., 2010). The existing design standards and guidelines do not presently incorporate provisions for addressing this specific type of failure.

Conversely, in lubricated conditions, friction between the contacting surfaces of the gears is reduced, facilitating heat dissipation and enhancing the strength of polymer gears. In lubricated conditions, the significance of subsurface stresses becomes more pronounced, making the gear surfaces more susceptible to pitting fatigue, as illustrated in Fig. 10.1D. Pitting fatigue refers to surface damage that occurs due to repeated contact stress cycles. This phenomenon explains why flank strength considerations specifically apply to lubricated polymer gears in design guidelines such as VDI 2736 (VDI-2736, 2014).

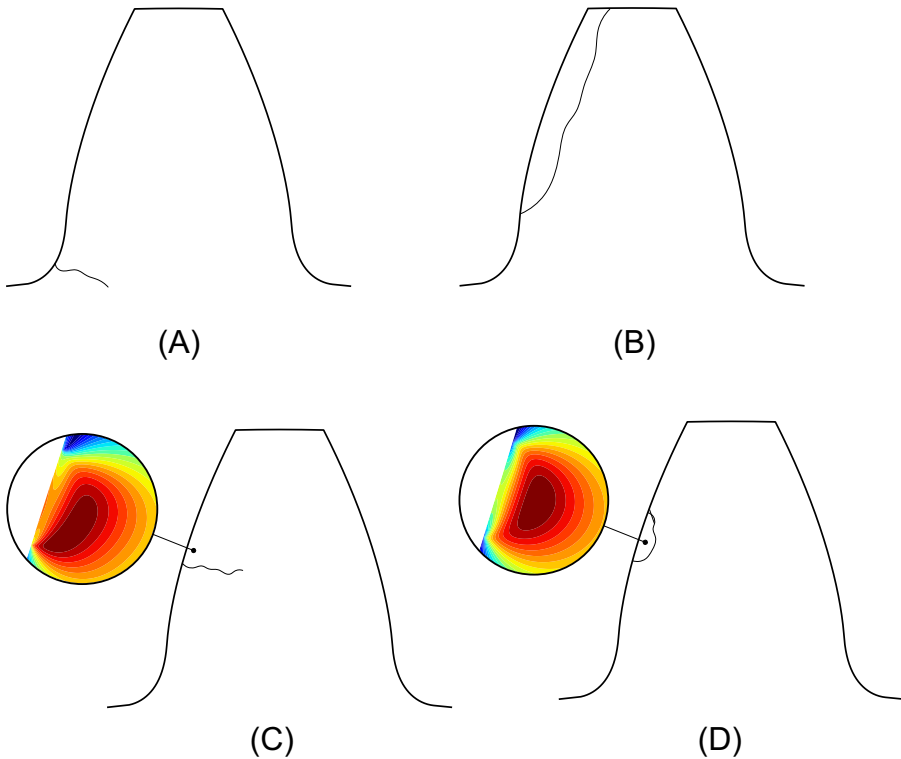


**Figure 10.1** Common polymer gear failures: (A) Root failure; (b) Wear; (C) Pitch line fracture - typically dry-run; (D) Pitting - typically lubricated.

Source: Adapted from Walton, D., & Shi, Y. W. W. (1989). A comparison of ratings for plastic gears. *Proceedings of the Institution of Mechanical Engineers, Part C: Journal of Mechanical Engineering Science*, 203, 31–33. [https://doi.org/10.1243/PIME\\_PROC\\_1989\\_203\\_083\\_02](https://doi.org/10.1243/PIME_PROC_1989_203_083_02).

Temperature plays a critical role in determining the performance and durability of polymer gears. The material temperature directly impacts the mechanical properties and dimensional stability of the polymer gear, making it a decisive factor in durability. Elevated temperatures can trigger a series of detrimental effects, leading to accelerated degradation, reduced strength, and increased wear rates in polymers, ultimately compromising the functionality of the gears (Kalin & Kupec, 2017; Mao et al., 2010). Thus, controlling and managing temperature becomes paramount in ensuring the long-term reliability and optimal performance of polymer gears.

Among the significant effects of temperature on polymer gear failures, one noteworthy consequence is the thermal softening of the material. As temperatures rise, the molecular structure of the polymer becomes more mobile, resulting in a decrease in mechanical strength and stiffness. Additionally, elevated temperatures induce thermal expansion in the polymer, leading to dimensional changes that can

impair the gear's meshing characteristics, thereby increasing friction and wear. To mitigate these adverse effects, careful consideration and implementation of effective temperature control strategies are imperative in the design and operation of polymer gears. In this regard, several design modifications have been proposed in the literature to address these issues (Fernandes et al., 2019; Hooton et al., 2023).

To properly design a polymer gear, the operating temperature should be well quantified. There are several analytical methods typically used to determine the bulk temperature of polymer gears (Hachmann & Strickle, 1966; Takanashi & Shoji, 1979a, 1979b; Mao, 1993; Takanashi & Shoji, 1980; VDI-2736, 2014). While the analytical methods are easy and fast to implement, they still present some noticeable limitations (Roda-Casanova & Fernandes, 2022). To overcome the limitations of the analytical methods, several numerical models have been proposed in the literature (Černe et al., 2020a; Fernandes et al., 2018; Li et al., 2018; Lu et al., 2020; Mao, 2007; Roda-Casanova & Sanchez-Marin, 2019).

The design of a polymer gear is a suitable optimization problem (Miler et al., 2020; Miler & Hoić, 2021; Tavčar et al., 2021) that requires a precise and fast quantification of its temperature during operation. For such purpose, the finite element model strategies are typically time-consuming and inadequate for the optimization problem under consideration and are better suited for verification of a smaller set of optimal designs. The following sections present a semianalytical modeling approach designed to provide a fast and accurate solution to the steady-state temperature field, making it a valuable tool for plastic gear design and optimization.

## 10.2 Typical examples of polymer gear pairings and corresponding operating conditions

In this section, two typical examples of polymer gear pairings and their corresponding operating conditions are presented. These case studies were carefully selected from available experimental results (Pogacnik & Tavcar, 2015; Singh et al., 2018) to validate the methods presented. Each case study explores different gear geometries, material pairings, and specific operating conditions, providing valuable insights into the performance and behavior of polymer gears under diverse scenarios.

Table 10.1 lists the gear geometries, material pairings, and specific operating conditions for each case study, including input speeds, input torques, and ambient temperatures. These conditions have been taken into account to comprehensively investigate their influence on polymer gear thermal behavior.

Table 10.2 provides the mechanical and thermal properties of the materials used in the case studies. Table 10.3 includes the properties of the surrounding medium (air), such as density, specific heat, and thermal conductivity. These air properties are considered to ensure accurate and reliable calculations, as the surrounding medium significantly affects the thermal convection of polymer gears.

**Table 10.1** Definition of case studies: gear geometries, materials, and operating conditions (Roda-Casanova & Fernandes, 2022).

Parameter	Plastic/plastic	Plastic/steel
Normal module, $m_n/\text{mm}$	1	2
Normal pressure angle, $\alpha_n/^\circ$	20	20
Face width, $b/\text{mm}$	6	8
Pinion tooth number, $z_1$	20	20
Wheel tooth number, $z_2$	20	20
Pinion profile shift, $x_1$	0	0
Wheel profile shift, $x_2$	0	0
Inner radius (shaft), $r_s/\text{mm}$	3	8
Addendum coefficient, $h_{aP}$	1	1
Deddendum coefficient, $h_{fP}$	1.25	1.25
Root radius coefficient, $\rho_{fP}$	0.25	0.25
Center distance, $a_w/\text{mm}$	20.05	40.00
Nominal input speed, $\omega_1/\text{rpm}$	1646	1200
Nominal input torque, $M_1/\text{Nm}$	0.59	2.00
Ambient temperature, $T_\infty/^\circ\text{C}$	23	29
Pinion material	POM <sup>a</sup>	POM
Wheel material	PA6 <sup>b</sup>	Steel
Coefficient of friction, $\mu$ (VDI-2736, 2014)	0.18	0.20

<sup>a</sup>polyoxymethylene<sup>b</sup>polyamide 6**Table 10.2** Thermal and mechanical properties of the gear materials (VDI-2736, 2014).

Parameter	Steel	POM	PA6
Density, $\rho/\text{kg/m}^3$	7850	1410	1135
Thermal conductivity, $\lambda/\text{W/m/K}$	52	0.28	0.29
Specific heat, $c/\text{J/kg/K}$	470	1470	1500
Young modulus at 20°C, $E/\text{GPa}$	206	2.9	1.8
Poisson ratio at 20°C, $\nu$	0.30	0.42	0.38

**Table 10.3** Thermal properties of the surrounding air at different temperatures (Roda-Casanova & Fernandes, 2022).

Property	23°C	29°C
Thermal conductivity, $\lambda_{air}/\text{W/m/K}$	$25.91 \times 10^{-3}$	$26.35 \times 10^{-3}$
Kinematic viscosity, $\nu_{air}/\text{m}^2/\text{s}$	$15.62 \times 10^{-6}$	$16.18 \times 10^{-6}$
Specific heat, $c_{air}/\text{J/kg/K}$	1006.92	1007.16
Density, $\rho_{air}/\text{kg/m}^3$	1.177	1.154

Through the comprehensive analysis of these typical examples of polymer gear pairings and their corresponding operating conditions, the relevant factors essential for establishing an accurate prediction of the polymer gear temperature are highlighted.

### 10.3 Thermal finite element model

The Fourier-Biot equation is a fundamental tool to model transient heat transfer in various systems (Çengel, 2003). When internal heat generation is negligible, it simplifies to the diffusion equation:

$$\nabla \cdot (\lambda \cdot \nabla T) = \rho \cdot c \cdot \frac{\partial T}{\partial t} \quad (10.1)$$

The diffusion equation describes how temperature changes over space and time. Blok (1963) observed that close-to-the-surface transient effects play a significant role in moving heat sources (Patir & Cheng, 1979; Wang & Cheng, 1980). However, beneath this thin thermal skin, transient effects become negligible, leading to a quasi-steady temperature solution as time progresses (Blok, 1963). In steady operating conditions with a constant heat source rate, the traditional Laplace equation applies:

$$\nabla \cdot (\lambda \cdot \nabla T) = 0 \quad (10.2)$$

The scalar field  $T$  is solely a function of position within the solid under analysis.

#### 10.3.1 Boundary conditions

The finite element model's geometric domain is defined by a single tooth, as depicted in Fig. 10.2, with the specific surface boundaries of interest identified.

Heat convection is assigned to the gear surfaces  $\Gamma_i$  ( $i = R, S, T, U$ ), as described by Eq. (10.3), while radiation effects are disregarded for the sake of simplicity. Given the focus on dry run conditions for the polymer gear, only convection within an air environment will be taken into account. For insights into lubricated conditions, the reader is directed to a previous work (Fernandes et al., 2018).

$$-\lambda \cdot \frac{\partial T}{\partial n} \Big|_{\Gamma_i} = h_{\Gamma_i} \cdot (T - T_{\infty}) \quad (10.3)$$

For the meshing flank represented by the boundary  $\Gamma_M$  in Fig. 10.2, both the time-averaged frictional heat flux  $\bar{q}_f$  and the heat convection are considered, as shown in Eq. (10.4).

$$-\lambda \cdot \frac{\partial T}{\partial n} \Big|_{\Gamma_M} = h_{\Gamma_M} \cdot (T - T_{\infty}) - \bar{q}_f \quad (10.4)$$

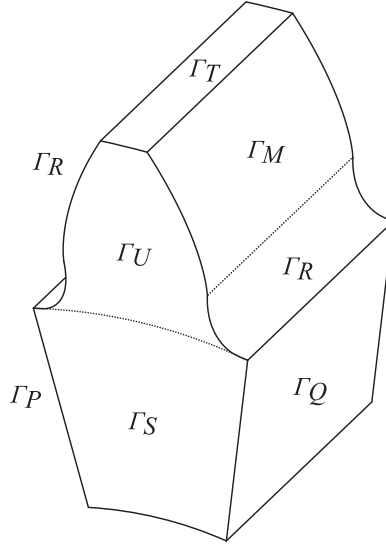


**Figure 10.2** Heat transfer problem geometric domain.

Assuming steady-state conditions, all teeth are expected to share an identical temperature field. Consequently, cyclic symmetry conditions need to be enforced on the boundaries  $\Gamma_P$  and  $\Gamma_Q$ . Those boundary conditions can be described by the Neumann boundary condition in Eq. (10.5) and the Dirichlet boundary condition outlined in Eq. (10.6).

$$\left. \frac{\partial T}{\partial n} \right|_{\Gamma_P} = \left. \frac{\partial T}{\partial n} \right|_{\Gamma_Q} \quad (10.5)$$

$$T_{\Gamma_P} = T_{\Gamma_Q} \quad (10.6)$$

The inner hole of the gear, where contact with the transmission shafts typically takes place, is treated as an adiabatic boundary, and heat conduction effects are disregarded ( $\partial T / \partial n = 0$ ). This simplification is well-justified considering the significant separation from the heat source (boundary  $\Gamma_M$ ) and the low thermal conductivity of the polymers (Fernandes et al., 2018; Roda-Casanova & Sanchez-Marin, 2019; Shunlei, 2010). However, Černe et al. (2020a) took a different approach by considering the contact between the shaft and the inner hole of the gear, thereby addressing the limitations of this assumption.

### 10.3.2 Convective heat transfer coefficients

The convective heat transfer coefficients are quite challenging to be accurately determined, being dependent on the cooling/lubrication method used on the gear system (Patir & Cheng, 1979).

The heat transfer coefficient resulting from convection is typically determined using Eq. (10.7).

$$h_{\Gamma_i} = \text{Nu} \cdot \frac{\lambda_{\text{air}}}{L_c} \quad (10.7)$$

The characteristic length  $L_c$  depends on the specific surface under consideration. For gears, the reference radius ( $r$ ), the tip radius ( $r_a$ ), the root radius ( $r_d$ ), the face width ( $b$ ), the normal tooth thickness over the reference circle ( $s_n$ ), and the tooth thickness over the tip circle ( $s_a$ ) are typically used. To calculate the Nusselt number ( $\text{Nu}$ ), the Eq. (10.8) is considered:

$$\text{Nu} = C_1 \cdot \text{Re}^{C_2} \cdot \text{Pr}^{C_3} \quad (10.8)$$

The Reynolds number ( $\text{Re}$ ) for each surface is determined according to Eq. (10.9) considering the air properties required for the Reynolds ( $\text{Re}$ ) and Prandtl ( $\text{Pr}$ ) numbers which are provided in Table 10.3.

$$\text{Re} = \frac{L_c \cdot v_{\text{air}}}{\nu_{\text{air}}} \quad (10.9)$$

The recent literature addressing the determination of heat transfer coefficients through convection on polymer gear tooth surfaces has been summarized in Table 10.4. Several authors have proposed different sets of coefficients, resulting in variations in the typical values of the constants  $C_1$ ,  $C_2$ , and  $C_3$ . These variations stem from the assumptions made regarding the flow pattern on each convection surface.

**Table 10.4** Nusselt exponents and surface characteristic length for each convective surface.

Source	Surface	$v_{\text{air}}$	$L_c$	$C_1$	$C_2$	$C_3$
(Fernandes et al., 2018)	$\Gamma_M$ (meshing)	$\omega \cdot r$	$r_a - r_d$	0.228	0.731	0.333
	$\Gamma_R, \Gamma_M$ (no meshing)		$r$	$0.127 \cdot \sqrt{m_h + 2}$	0.500	0.500
	$\Gamma_S, \Gamma_T, \Gamma_U$		$r$	$0.308 \cdot \sqrt{m_h + 2}$	0.500	0.500
(Černe et al., 2020a)	$\Gamma_M, \Gamma_R, \Gamma_T$	$\omega \cdot r$	$2 \cdot (r_a - r_d)$	3.800	0.200	0.333
	$\Gamma_S$		$r$	0.326	0.500	0.000
	$\Gamma_U$		$s_n$	0.664	0.500	0.333
(Roda-Casanova et al., 2023)	$\Gamma_M$	$\omega \cdot r$	$b/2$	0.089	0.748	0.333
	$\Gamma_R$		$b/2$	0.027	0.829	0.333
	$\Gamma_S$		$r$	0.174	0.630	0.333
	$\Gamma_U$		$s_n$	0.196	0.605	0.333
	$\Gamma_T$	$\omega \cdot r_a$	$s_a$	0.108	0.645	0.333

Fernandes et al. (2018) based their findings on the solution for a rotating disk in air as proposed by Hartnett and Deland (1961). This solution is particularly representative of what happens on gear sides  $\Gamma_S$  when a laminar flow exists. According to Hartnett and Deland (1961) the heat transfer coefficient is independent of the disk radius (or gear side radius) if the Reynolds number (Re) is below  $2 \times 10^5$ . A similar consideration was made for the surfaces  $\Gamma_U$  and  $\Gamma_T$ . However, for the surface  $\Gamma_R$ , the constant  $C_1$  was adjusted following the suggestions of Shunlei (2010). It is worth acknowledging that while the results obtained for surfaces  $\Gamma_R$ ,  $\Gamma_U$ , and  $\Gamma_T$  may show good correlation with the experimental data, the underlying assumption of a rotating disk in the air as a representation of these gear surfaces is a simplification of the actual problem. In reality, the flow patterns may differ significantly from those of a rotating disk in the air (Roda-Casanova et al., 2023).

Černe et al. (2020a) based the convective heat transfer model on three distinctive reference surfaces. The coefficients proposed by Knudsen et al. (1959), which were obtained for surfaces resembling a semicylindroid (with a radius equal to the tooth depth) positioned inside an air crossflow (Roda-Casanova et al., 2023), are used for the calculation of convective heat transfer on the surfaces  $\Gamma_M$ ,  $\Gamma_R$ , and  $\Gamma_T$ . For the tooth sides (surface  $\Gamma_U$ ), the surfaces were considered as plates with the airflow parallel to them, using the solution proposed by Holman (1986), which is valid for Reynolds numbers under  $5 \times 10^5$ . Finally, the gear sides (surface  $\Gamma_S$ ) were considered as a disk rotating in quiescent air following the solution obtained by Millsaps and Pohlhausen (Millsaps & Pohlhausen, 1952). These coefficients are recommended for Reynolds numbers below  $2 \times 10^6$  (Roda-Casanova et al., 2023).

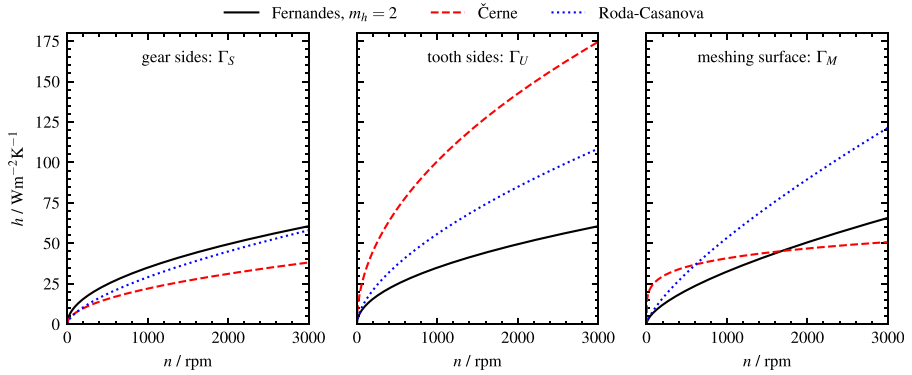
Roda-Casanova et al. (2023) introduced a comprehensive set of Nusselt number coefficients, as illustrated in Table 10.4, derived from an extensive computational fluid dynamics (CFD) analysis. The CFD model was designed to provide a deep and insightful examination of the unique characteristics associated with each convective surface. Despite the limitations of the study with respect to the relatively narrow range of speeds and gear geometries analyzed, the methodology employed proved to be highly effective in quantifying the heat transfer coefficients in dry-run polymer gears.

Fig. 10.3 provides a comparative analysis of heat transfer coefficients based on the methodologies proposed by the different authors. The heat transfer coefficient calculated by Fernandes and Roda-Casanova coefficients for the gear sides consistently exhibits a similar magnitude. In the case of the tooth sides, Roda-Casanova and Černe employed a specific set of coefficients, while Fernandes applied the same methodology used for the gear sides, resulting in significantly higher values for Černe and Roda-Casanova.

### 10.3.3 A remark for the meshing surface

The heat transfer coefficient for the tooth flank boundary  $\Gamma_M$  during meshing is determined using Eqs. (10.7) and (10.8), with the coefficients  $C_1 = 0.228$ ,  $C_2 = 0.731$ , and  $C_3 = 0.333$  proposed by Fernandes et al. (2018) based on the work of Handschuh (Handschuh, 1993; Holman, 1986).





**Figure 10.3** Comparison of heat transfer coefficients (plastic/steel example).

For the remaining of the cycle, a more accurate estimate of the heat transfer coefficient at the tooth flank boundary can be achieved by assuming it is equal to the boundary  $\Gamma_R$ . Under steady-state conditions, the overall heat transfer at the boundary  $\Gamma_M$  can then be represented by Eq. (10.10).

$$h_{\Gamma_M} = \frac{1}{z} \cdot h_{\Gamma_M} + \frac{z-1}{z} \cdot h_{\Gamma_R} \quad (10.10)$$

This assumption is based on the understanding that the convection conditions during the meshing time are different from those observed on the nonmeshing boundary, which occurs when  $\Gamma_M$  is outside the meshing region for the majority of the time during a gear rotation. For a comprehensive comparison between the results obtained through Fernandes convective model and those derived from other proposed models, please refer to Fig. 10.3. It is worth noting that Fernandes method presents smaller values at lower speeds compared to Černe's model. However, as the speed increases, Fernandes model yields larger values. The heat transfer coefficient values for the meshing surface predicted by Roda-Casanova's method consistently exhibit higher values in comparison with the other approaches across most of the considered speed range.

### 10.3.4 Gear geometry definition and finite element method (FEM) mesh creation

Following what is recommended by Maag Gear Company Ltd (1990), consider the involute curve  $r^i$  represented in Fig. 10.4A. The point of that curve that belongs to the reference circle  $r$  is coincident with the ordinate axis considered. The curve is given by the following equation:

$$r^i = r \cdot \begin{Bmatrix} \sin \varphi - \varphi \cdot \cos \alpha_n \cdot \cos(\varphi + \alpha_n) \\ \cos \varphi + \varphi \cdot \cos \alpha_n \cdot \sin(\varphi + \alpha_n) \\ 0 \end{Bmatrix}, \quad \varphi \in [\varphi_i, \tan \alpha_a - \tan \alpha_n] \quad (10.11)$$

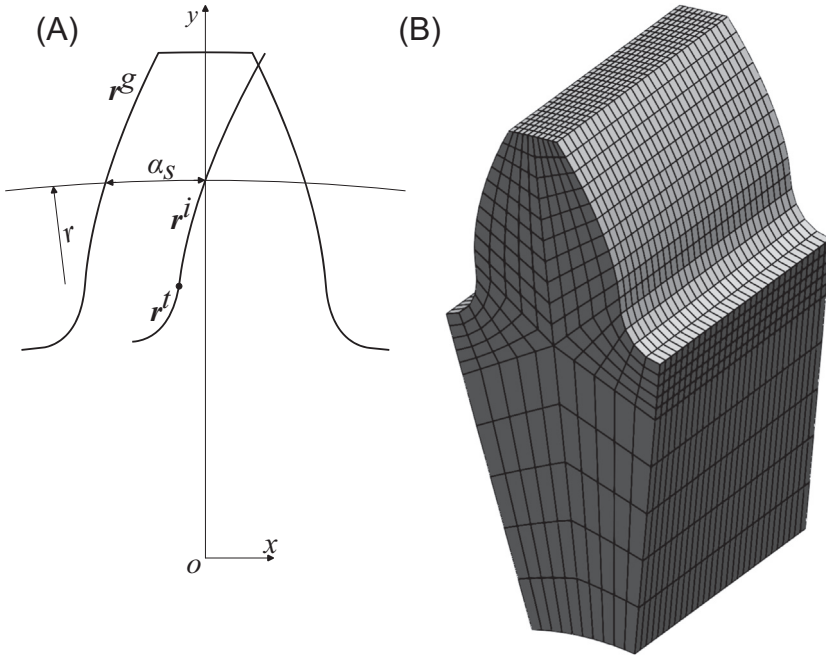


**Figure 10.4** Definition of gear tooth geometry for load sharing calculation and finite element mesh creation.

The incidence angle  $\alpha_a$  of the involute profile over the tip radius ( $r_a$ ) is determined by:

$$\alpha_a = \arccos\left(\frac{r_b}{r_a}\right) \quad (10.12)$$

The involute curve is valid within a specific range of the angle  $\varphi$ , starting from the interception point between the involute and trochoid curves ( $\varphi_i$ ) and ending at the tip circle. The angle  $\varphi_i$  can be determined by intersecting both the involute and trochoid curves.

The vector equation representing the trochoid coordinates of the tooth root is given by:

$$\mathbf{r}^t = \begin{pmatrix} r \cdot \sin\varphi + \left( \frac{-r \cdot \varphi - A}{\cos\delta} + \rho_{fp} \cdot m \right) \cdot \cos(\varphi + \delta) \\ r \cdot \cos\varphi + \left( \frac{-r \cdot \varphi - A}{\cos\delta} + \rho_{fp} \cdot m \right) \cdot \sin(\varphi + \delta) \\ 0 \end{pmatrix}, \quad \varphi \in \left[ -\frac{A}{r}, \varphi_i \right] \quad (10.13)$$

In this case,  $r$  represents the reference circle radius,  $\varphi$  is the angle parameter within the specified range, and  $A$ ,  $\delta$ , and  $\rho_{fp}$  depend on the generating rack geometry. To determine the parameters  $A$ ,  $B$ , and  $\delta$ , the rack points equations are considered as follows:

$$A = (h_{fp} - x) \cdot m_n \cdot \tan \alpha_n + \rho_{fp} \cdot m_n \cdot \frac{1 - \sin \alpha_n}{\cos \alpha_n} \quad (10.14)$$

$$B = (h_{fp} - x - \rho_{fp}) \cdot m_n \quad (10.15)$$

$$\delta = \arctan \left( \frac{B}{-r \cdot \varphi - A} \right) \quad (10.16)$$

In Eqs. (10.14), (10.15), and (10.16),  $x$  is the gear profile shift, and  $h_{fp}$  and  $\rho_{fp}$  are the coefficients of the dedendum and the fillet radius, respectively.

The involute and trochoid that constitute the final tooth geometry ( $\mathbf{r}^g$ ) are obtained by rotating the involute ( $\mathbf{r}^i$ ) and trochoid ( $\mathbf{r}^t$ ) curves by an angle  $\alpha_s$  representing the rotation angle that is related to the tooth arc length ( $s_n$ ) over the reference circle:

$$\alpha_s = \frac{s_n}{2 \cdot r} \quad (10.17)$$

The transformation matrix is then represented by:

$$\mathbf{T} = \begin{bmatrix} \cos \alpha_s & -\sin \alpha_s & 0 \\ \sin \alpha_s & \cos \alpha_s & 0 \\ 0 & 0 & 1 \end{bmatrix} \quad (10.18)$$

Moreover, the dedendum circle ( $\mathbf{r}^d$ ) and addendum circle ( $\mathbf{r}^a$ ) are given in their final positions as follows:

$$\mathbf{r}^{d,a} = r_{d,a} \cdot \begin{Bmatrix} \sin \varphi_{d,a} \\ \cos \varphi_{d,a} \\ 0 \end{Bmatrix}, \quad \varphi_d \in \left[ -\frac{\pi}{z}, \arctan \left( \frac{r_x^t}{r_y^t} \right) - \alpha_s \right] \vee \varphi_a \in \left[ -\frac{s_a}{2 \cdot r_a}, 0 \right] \quad (10.19)$$

Here,  $r_x^t$  and  $r_y^t$  denote the point's abscissa and ordinate coordinates of the trochoid curve that connects with the dedendum circle.

The left side of the final tooth profile (corresponding to the negative abscissa on the axis system used) is derived by concatenating the previously defined curves:

$$\mathbf{r}^g = (\mathbf{r}^d, \mathbf{T} \times \mathbf{r}^t, \mathbf{T} \times \mathbf{r}^i, \mathbf{r}^a) \quad (10.20)$$

On the contrary, the right side of the tooth profile can be generated by ensuring positive abscissa coordinates. The methodology presented for creating tooth geometry has proven particularly beneficial for plastic gears without profile modifications. Although these equations can be adapted for profile modifications, a rack generation method as proposed by Litvin and Fuentes (2004) may provide a simpler and more efficient solution.

Following the generation of tooth geometry, the subsequent step entails creating a finite element mesh, following a methodology similar to that proposed by Argyris (Argyris et al., 2002; Roda-Casanova & Sanchez-Marin, 2019). By employing the Argyris method, which is well-established and widely used in the gear field, the meshing procedure ensures the appropriate resolution and quality of the finite elements, leading to reliable and precise results. An illustrative tooth mesh is depicted in Fig. 10.4B. This process involved extruding the geometry along the face width, resulting in a 3D finite element mesh.

## 10.4 Frictional heat flux

In the analysis of polymer gears, understanding the heat generation within the gear meshing process is crucial for predicting performance and ensuring reliable operation (Koffi et al., 1985). One important aspect of this analysis is to determine the frictional heat flux, which represents the conversion of meshing power loss into heat.

Following the Coulomb law of friction, the power loss of a contact pair along the path of contact can be calculated by:

$$P_f(\xi) = F_n(\xi) \cdot \mu(\xi) \cdot v_g(\xi) \quad (10.21)$$

Here,  $F_n$  is the normal load,  $\mu$  is the coefficient of friction, and  $v_g$  is the absolute sliding speed.

Building upon the same principle used for calculating power loss, the frictional heat flux can be obtained based on Hertz pressure distribution. To calculate the contact pressure distribution  $p(\xi, x)$ , a parabolic pressure distribution within the contact area is considered. The equation describing this distribution is as follows:

$$p(\xi, x) = p_0(\xi) \cdot \sqrt{1 - \left(\frac{x}{a_H(\xi)}\right)^2} \quad (10.22)$$

The moving heat source is represented in Fig. 10.5A for two distinct positions  $\xi_m$  and  $\xi_n$ , meaning that the heat flux is both function of the meshing position ( $\xi$ ) and position ( $x$ ) within the Hertzian contact width  $2 \cdot a_H(\xi)$ . The frictional heat flux, denoted as  $q_f(\xi, x)$ , can be calculated using the following equation:

$$q_f(\xi, x) = \gamma \cdot \chi_i(\xi) \cdot p(\xi, x) \cdot \mu(\xi) \cdot v_g(\xi) \quad (10.23)$$

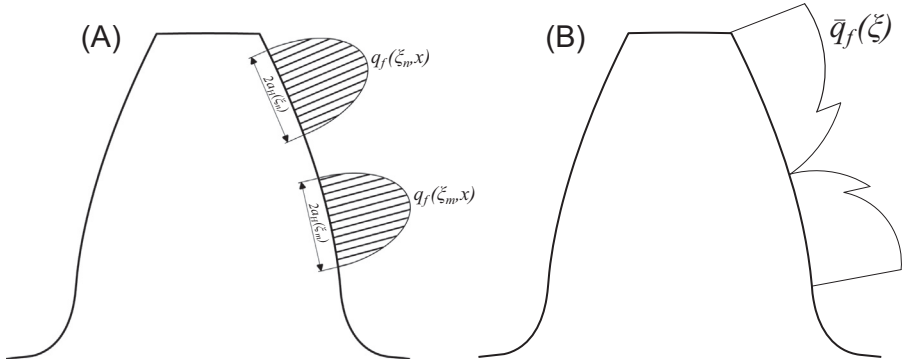


**Figure 10.5** Frictional heat flux on the meshing tooth surface.

In Eq. (10.23),  $\gamma$  represents the conversion of friction into heat transferred to the solids, typically ranging between 0.9 and 0.95 (Luo & Li, 2016). For the sake of simplicity, it will be assumed  $\gamma = 1$  in the subsequent analysis. The term  $\chi_i$  represents the heat partition factor calculated for the pinion and wheel flanks.

In traditional gear rating standards, Hertz theory is commonly used to estimate the contact stress in line contacts. However, the applicability of Hertz's theory to polymer gears is limited due to the assumptions of infinitesimal strains as well as the presence of tooth profile modifications. Nonetheless, it is important to note that for a steady-state model, it will be demonstrated that Hertz's theory is not explicitly needed.

Hertz's theory provides a basic equation for the maximum contact pressure, given as:

$$p_0(\xi) = \sqrt{\frac{F_n(\xi) \cdot E(T)}{\pi \cdot b \cdot R(\xi)}} \quad (10.24)$$

In this equation,  $E$  is the effective Young's modulus,  $b$  is the common gear face width, and  $R(\xi)$  is the equivalent radius of curvature at each meshing position. The effective Young's modulus, which for polymeric materials is dependent on the operating temperature  $T$ , is given by Eq. (10.25).

$$\frac{1}{E(T)} = \frac{1 - \nu_1(T)^2}{E_1(T)} + \frac{1 - \nu_2(T)^2}{E_2(T)} \quad (10.25)$$

The equivalent radius of curvature that varies with the meshing position is:

$$\frac{1}{R(\xi)} = \frac{1}{R_1(\xi)} + \frac{1}{R_2(\xi)} \quad (10.26)$$

The half-width for a Hertzian line contact, denoted as  $a_H(\xi)$ , is given by:

$$a_H(\xi) = \sqrt{\frac{4 \cdot F_n(\xi) \cdot R(\xi)}{\pi \cdot b \cdot E(T)}} \quad (10.27)$$

To determine the time-averaged frictional heat flux needed for a steady-state thermal analysis, the friction energy  $E_f$  for each meshing position is divided by the time it takes to complete one running cycle (one rotation)  $t_i = \frac{2\pi}{\omega_i}$ . The expression for the time-averaged heat flux, denoted as  $\bar{q}_f(\xi)$ , is:

$$\bar{q}_f(\xi) = \frac{E_f(\xi)}{t_i} = \frac{\frac{1}{v_{ri}(\xi)} \cdot \int_{-a_H(\xi)}^{a_H(\xi)} q_f(\xi, x) dx}{t_i} \quad (10.28)$$

Here,  $\omega_i$  denotes the angular speed and  $v_{ri}$  is the rolling speed. By replacing the known terms into Eq. (10.28), the following expression is obtained:

$$\bar{q}_f(\xi) = \frac{\omega_i}{2 \cdot \pi \cdot v_{ri}(\xi)} \cdot \chi_i(\xi) \cdot \mu(\xi) \cdot v_g(\xi) \cdot p_0(\xi) \cdot \underbrace{\int_{-a_H(\xi)}^{a_H(\xi)} \sqrt{1 - \left(\frac{x}{a_H(\xi)}\right)^2} dx}_{\frac{1}{2}\pi \cdot a_H(\xi)} \quad (10.29)$$

By solving the integral presented in Eq. (10.29) and eliminating common terms, a simplified equation that is solely dependent on the meshing position  $\xi$  is achieved:

$$\bar{q}_f(\xi) = \frac{1}{2 \cdot \pi \cdot b \cdot R_i(\xi)} \cdot \chi_i(\xi) \cdot \underbrace{F_n(\xi) \cdot \mu(\xi) \cdot v_g(\xi)}_{P_f(\xi)} \quad (10.30)$$

Here,  $R_i$  is the curvature radius of the element of interest (pinion or wheel). Note that the only remaining factor originating from the application of Hertz theory is the face width  $b$ . The typical shape of the time-averaged frictional heat flux after disregarding tooth deflection may be observed in Fig. 10.5B.

#### 10.4.1 Heat partition factor

Heat generated in frictional contacts is often distributed unevenly between the contacting surfaces, a distribution influenced by material properties and relative speeds (Gurskii & Chichinadze, 2007). Several efforts have been made from Bowden and Ridler (1936) to Blok (1963) to quantify the partitioning of frictional heat flux between these surfaces. Sharron proposed the equation (Gurskii & Chichinadze, 2007):

$$\chi_i = \frac{e_i}{e_1 + e_2} \quad (10.31)$$

Here, the effusivity ( $e_i$ ) of each contacting material is calculated using Eq. (10.32):

$$e_i = \sqrt{k_i \cdot c_i \cdot \rho_i} \quad (10.32)$$

However, Blok emphasized the crucial role of surface speeds in the heat distribution due to a moving heat source (Blok, 1963). Consequently, Blok's Eq. (10.33) has gained widespread acceptance and frequent application in the field of gear literature.

$$\chi_i = \frac{e_i \cdot \sqrt{v_{ri}}}{e_1 \cdot \sqrt{v_{r1}} + e_2 \cdot \sqrt{v_{r2}}} \quad (10.33)$$

Following the discussion by Roda-Casanova and Fernandes (2022) on the implicit heat partition coefficient included in the VDI 2736 temperature prediction equation, it can be inferred that, for similar gear geometry and materials, a value of  $\chi_i = 0.5$  is expected. However, when dealing with plastic/steel gears, a different value of  $\chi_i = 0.208$  was found.

Fig. 10.6 illustrates a comparison of the aforementioned methods for both examples of gear pairs. For plastic/plastic gear pairs, the heat partition coefficient  $\chi_i$  varies between 0.35 and 0.7 when using the Blok equation. In contrast, the values obtained using VDI 2736 or the Sharron method are close to 0.5. Interestingly, the coefficient from the Sharron equation is similar to the one found by Černe et al. (2020a) for the same gear example. For the plastic/steel gear pairing, VDI 2736 gives a significantly higher value compared to both the Sharron and Blok coefficients. One plausible explanation for this discrepancy is the neglected hysteresis losses in the VDI 2736 method. Roda-Casanova and Fernandes (2022) demonstrated that incorporating hysteresis losses into the analytical method proposed by

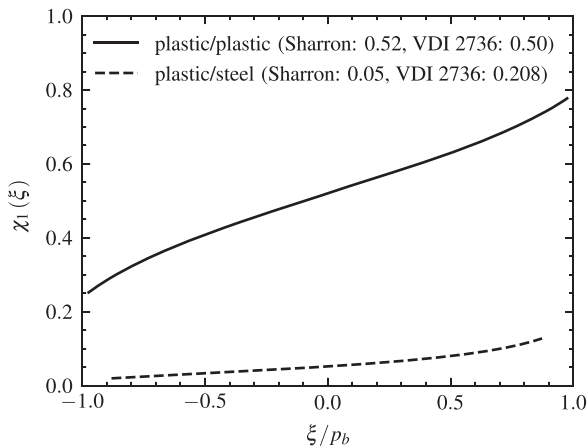


**Figure 10.6** Heat partition coefficient along the path of contact.

Takanashi, along with the Blok coefficient, yields similar results to those obtained using VDI 2736. This is particularly important because hysteresis losses may be relevant in polymer gears (Roda-Casanova & Fernandes, 2022).

### 10.4.2 Load sharing ratio

Assuming a frictionless contact, the normal load over a single tooth pair in contact for each meshing position in cylindrical gears can be determined using the following equation:

$$F_n(\xi) = Y(\xi) \cdot F_{bt} \quad (10.34)$$

In Eq. (10.34), the normal load ( $F_n$ ) is calculated by multiplying the coefficient  $Y(\xi)$  with the base tangential load ( $F_{bt}$ ). The coefficient  $Y(\xi)$  represents the load sharing ratio, which determines how the load is distributed between the meshing gear teeth pairs.

In the realm of predicting load-sharing ratios for metallic cylindrical gears, the literature offers a range of methods for analysis, encompassing both analytical (Pedrero et al., 2010; Weber & Banaschek, 1953), numerical (Cooley et al., 2016), or approximate analytical techniques (Marques et al., 2021). However, when we shift our focus to nonmetallic gears, we find that the effort invested in such analyses has been limited. Analytical models for nonmetallic gears are notably limited within the literature (Letzelter et al., 2009; Zhiliang et al., 2021). In contrast, the reliance on finite element analysis-based models is more prevalent (Karimpour et al., 2010). In the specific context of polymer gears, Takanashi and Shoji (1979) have made noteworthy use of models initially proposed by Timoshenko and Baud (1926) and Caldwell to predict the hysteresis losses (Roda-Casanova & Fernandes, 2022).

In many analytical approaches, a crucial step involves the quantification of mesh stiffness, a fundamental aspect when evaluating the behavior of cylindrical gears. To determine the mesh stiffness of a cylindrical gear, the most typical analytical method is based on the minimization of potential energy, as elucidated in works such as Pedrero et al. (2010). This approach requires a comprehensive assessment of various contributions to the mesh stiffness. For an in-depth exploration and comparison of these methodologies, readers are directed to a comprehensive review (Marafona et al., 2021).

To calculate the gear mesh stiffness, the tooth geometry, as illustrated in Fig. 10.7, is considered. The axis system is conveniently aligned with the gear's center and the ordinate axis corresponds to the vertical axis of symmetry for the tooth. When considering a contact point (denoted as point  $C$ ), the angle formed between the radius originating from point  $C$  (designated as  $r_C$ ) and the ordinate axis can be expressed as:

$$\gamma_C = \frac{s_n}{2 \cdot r} + \text{inv}\alpha_n - \text{inv}\alpha_M \quad (10.35)$$



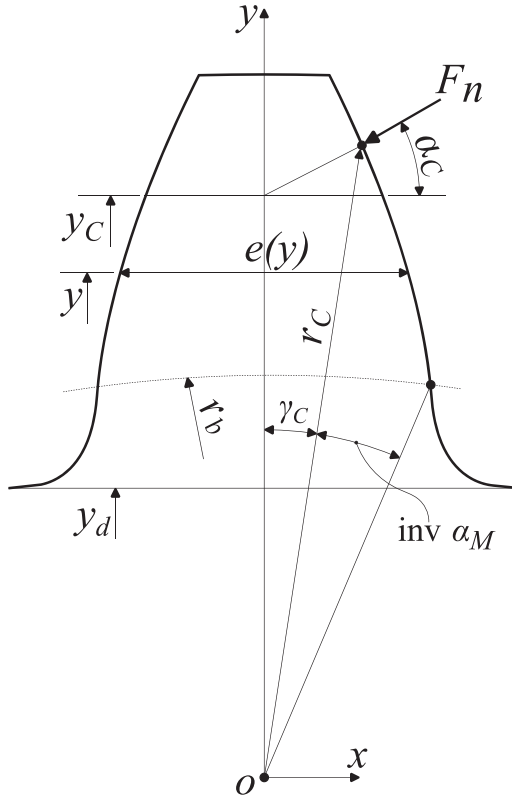


**Figure 10.7** Gear geometry for mesh stiffness calculation.

According to the properties governing the involute profile of a circle with a base radius  $r_b$ , the angle of incidence for the profile at point  $C$  can be determined as:

$$\alpha_M = \arccos\left(\frac{r_b}{r_C}\right) \quad (10.36)$$

The angle between the normal load  $F_n$  and the abscissa axis can be defined as:

$$\alpha_C = \alpha_M - \gamma_C \quad (10.37)$$

For any chosen value of  $y$ , the tooth dimension along the abscissa axis is denoted as  $e(y)$ . Additionally, the value of  $y_C$  associated with any given contact point with a radius  $r_C$  is determined through the following equation:

$$y_C = \frac{r_b}{\cos \alpha_C} \quad (10.38)$$

For a pair of gear teeth, the total stiffness ( $k_i$ ) is given by Eq. (10.39):

$$k_i = \left( \frac{1}{k_{t1}} + \frac{1}{k_{f1}} + \frac{1}{k_{t2}} + \frac{1}{k_{f2}} + \frac{1}{k_H} \right)^{-1} \quad (10.39)$$

The tooth stiffness, as described by Eq. (10.39), comprises the tooth structural stiffness ( $k_{ti}$ ), the gear foundation stiffness ( $k_{fi}$ ), and the contact stiffness ( $k_H$ ). The tooth structural stiffness is composed of three components: bending stiffness, compressive stiffness, and shear stiffness, as shown in Eq. (10.40).

$$\begin{aligned} \frac{1}{k_{ti}} = & \underbrace{\frac{12}{E_i \cdot b_i} \cdot \int_{r_d}^{y_C} \frac{(y_C - y)^2 \cdot \cos^2 \alpha_C}{e^3(y)} dy}_{\text{bending}} + \underbrace{\frac{1}{E_i \cdot b_i} \cdot \int_{r_d}^{y_C} \frac{\sin^2 \alpha_C}{e(y)} dy}_{\text{compression}} \\ & + \underbrace{\frac{C_s}{G_i \cdot b_i} \cdot \int_{r_d}^{y_C} \frac{\cos^2 \alpha_C}{e(y)} dy}_{\text{shear}} \end{aligned} \quad (10.40)$$

In the preceding equation,  $E_i$  and  $G_i$  denote the elastic properties of the gear element in question (pinion or wheel), while  $b_i$  represents the face width and  $C_s$  is a constant value set at 1.2.

The foundation stiffness was estimated with Eq. (10.37) proposed by Sainsot et al. (2004).

$$\frac{1}{k_{fi}} = \frac{\cos^2 \alpha_C}{E_i \cdot b_i} \left[ X_L \cdot \left( \frac{y_C - r_d}{2 \cdot r_b \cdot \theta_f} \right) + X_M \cdot \left( \frac{y_C - r_d}{2 \cdot r_b \cdot \theta_f} \right) + X_P \cdot (1 + X_Q \cdot \tan^2 \alpha_C) \right] \quad (10.41)$$

In the previous equation,  $r_d$  represents the dedendum radius while the angle  $\theta_f$  is given by:

$$\theta_f = \frac{1}{z} \cdot \left[ \frac{\pi}{2} + 2 \cdot \tan \alpha_n \cdot (h_{fp} - \rho_{fp}) + \frac{2 \cdot \rho_{fp}}{\cos \alpha_n} \right] \quad (10.42)$$

The parameters  $X_L$ ,  $X_M$ ,  $X_P$  and  $X_Q$  are given by the curve fitted Eq. (10.43), with coefficients given by Table 10.5.

$$X_j = \frac{A_j}{\theta_f^2} + B_j \cdot \left( \frac{r_d}{r_s} \right)^2 + \frac{C_j \cdot r_d}{\theta_f \cdot r_s} + \frac{D_j}{\theta_f} + E_j \cdot \frac{r_d}{r_s} + F_j \text{ with } j = L, M, P, Q \quad (10.43)$$

Additionally, the contact stiffness ( $k_H$ ) can be determined using the Hertz theory, as shown in Eq. (10.44). This simplified equation was employed to streamline the

**Table 10.5** Polynomial coefficients obtained for Eq. (10.39).

$j$	$A_j \times 10^5$	$B_j \times 10^3$	$C_j \times 10^4$	$D_j \times 10^3$	$E_j$	$F_j$
$L$	-5.5740	-1.9986	-2.3015	4.7702	0.0271	6.8045
$M$	60.1110	28.1000	-83.4310	-9.9256	0.1624	0.9086
$P$	-50.9520	185.5000	0.0538	53.3000	0.2895	0.9236
$Q$	-6.2042	9.0889	-4.0964	7.8297	-0.1472	0.6904

Source: From Sainsot, P., Velex, P., & Duverger, O. (2004). Contribution of gear body to tooth deflections—a new bidimensional. *Journal of Mechanical Design*, 126(4), 748–752.

implementation and avoid additional iterative procedures. Nevertheless, numerous alternative approaches are available (Sainsot & Velex, 2020; Zhiliang et al., 2021).

$$\frac{1}{k_H} = \frac{4 \cdot (1 - \nu^2)}{\pi \cdot E(T) \cdot b_{\min}} \quad (10.44)$$

The displacements of the teeth under load cause the gear to have premature and extended contact, which is particularly relevant in the case of plastic gears (Karimpour et al., 2010). To consider the contact outside the path of contact (Singh & Houser, 1994), the concept of separation distance, as described by (Munro et al., 1999; Hsiang et al., 1993), may be considered. Eqs. (10.45–10.49) should be used to calculate the separation distance  $S_i$  of the pinion ( $i = 1$  and  $j = 2$ ) during the approach phase and the wheel ( $i = 2$  and  $j = 1$ ) during the recess phase:

$$S_i = \Delta_i \cdot r_{bi} \quad (10.45)$$

The separation angle  $\Delta_i$  is calculated with:

$$\Delta_i = \theta_i + \arctan\left(\frac{r_{aj} \cdot \sin\beta_j}{a_w - r_{aj} \cdot \cos\beta_j}\right) - \arctan\left(\frac{r_{aj} \cdot \sin(\theta_j + \beta_j)}{a_w - r_{aj} \cdot \cos(\theta_j + \beta_j)}\right) + \text{inv}\rho_i - \text{inv}\gamma_i \quad (10.46)$$

Here,  $\theta_i$  and  $\theta_j$  are, respectively, the rotation angle for the tooth that is approaching the path of contact or leaving the path of contact,  $r_{aj}$  is the tip radius, and  $a_w$  is the working center distance while the remaining angles are calculated with Eqs. (10.47–10.49).

$$\beta_j = \arccos\left(\frac{r_{bj}}{r_{aj}}\right) - \alpha_{tw} \quad (10.47)$$

Here,  $\alpha_{tw}$  represents the working pressure angle.

$$\rho_i = \arccos\left(\frac{r_{bi}}{\sqrt{[r_{aj} \cdot \sin(\theta_j + \beta_j)]^2 + [a_w - r_{aj} \cdot \cos(\theta_j + \beta_j)]^2}}\right) \quad (10.48)$$

$$\gamma_i = \arccos \left( \frac{r_{bi}}{\sqrt{[r_{aj} \cdot \sin \beta_j]^2 + [a_w - r_{aj} \cdot \cos \beta_j]^2}} \right) \quad (10.49)$$

The separation distance for the wheel during the approach phase ( $i = 1$  and  $j = 2$ ) and for the pinion ( $i = 2$  and  $j = 1$ ) during the recess phase can be obtained using the following equation:

$$S_j = \theta_j \cdot r_{bj} - (\theta_i - \Delta_i) \cdot r_{bi} \quad (10.50)$$

In the context of metallic gears, determining the actual approach and recess separation distances entails averaging the separation distance values obtained for the pinion and wheel using the aforementioned equations (Hsiang et al., 1993). However, in the case of plastic gears where deformations are more substantial, a specific method is necessary to estimate the actual separation distance, taking into account the relative stiffness of the engaged teeth. In cases with an equal number of teeth, the average of pinion and wheel separation distances is adequate. For gear systems with different tooth ratios, it is recommended to use Yelle's work (Yelle & Burns, 1981) for further guidance on this matter.

The load sharing ratio, denoted as  $Y(\xi)$ , can be determined using Eq. (10.51). This calculation requires first establishing the values of  $k_i$  for the tooth pair under examination, as well as for the preceding and succeeding tooth pairs, denoted as  $k_j$  (Marafona et al., 2023; Zhiliang et al., 2021).

$$Y(\xi) = \frac{k_i + k_i \cdot \sum \frac{k_j \cdot S_i}{F_n}}{k_i + \sum k_j} \quad (10.51)$$

The previous equation is implemented considering a frictionless contact for the mesh stiffness calculation. To include the friction effects over the load-sharing ratio calculation, the following modification is typically made (Reimann et al., 2019):

$$Y_\mu(\xi) = Y(\xi) \cdot \frac{r_b}{r_b + \sqrt{r_C^2 - r_b^2} \cdot \mu(\xi) \cdot \text{sign}(v_g)} \quad (10.52)$$

The sign of the sliding speed is obtained by:

$$\text{sign}(v_g) = \frac{v_{r1}(\xi) - v_{r2}(\xi)}{v_g(\xi)} \quad (10.53)$$

In Fig. 10.8, a comparison is made between the proposed method and the FEM results, with both a frictionless load-sharing solution (Eq. (10.51)) and the frictional load-sharing ratio (Eq. (10.52)) being incorporated. The 2D finite element analysis was implemented following a strategy akin to the one utilized in Zorko et al. (2019).

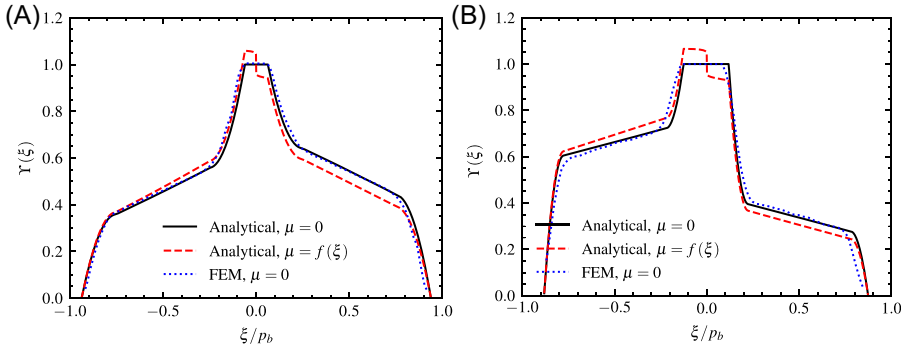


**Figure 10.8** Comparative analysis of load sharing ratio calculation using analytical and FEM methods.

However, for a more accurate representation of actual gear behavior, the full gears were modeled. A penalty contact formulation was employed, and the finite element mesh was composed of 8-node quadratic plane stress elements (CPS8), which underwent an h-refinement procedure to ensure result accuracy. The FEM results were postprocessed using a Savitzky-Golay filter (Cooley et al., 2016) to improve curve smoothness and eliminate minor noise. The results reveal a good agreement between the FEM results and the proposed analytical model. Taking into consideration the limitations of the previously proposed model (Fernandes et al., 2018), the incorporation of a realistic load-sharing ratio with consideration of the contact outside the theoretical path of contact should result in an improved temperature field prediction.

### 10.4.3 Coefficient of friction

The coefficient of friction is often treated as a constant value along the path of contact for the sake of simplification. This approximation is particularly accurate in lubricated contacts where the coefficient of friction tends to be small, as demonstrated by previous works (Fernandes et al., 2015, 2014, 2016). This simplification is also prevalent in most of the models presented in the literature for polymer gears, including those by Fernandes et al. (2018), Roda-Casanova and Sanchez-Marin (2019), and Černe et al. (2020a).

In the case of polymer gears, the average coefficient of friction is typically sourced from *VDI-2736 Blatt 2: Thermoplastic Gear Wheels - Cylindrical Gears-* (2013). However, equations are available to predict the local coefficient of friction. Takanashi and Shoji (1981) conducted twin-disk tests with various material combinations and lubrication conditions, proposing a curve-fitting equation based on the experimental data. Miler et al. (2019) and Yangshou Xiong and Zongshan (2023) have also used Eq. (10.54) to predict the local coefficient of friction. The equation aims to capture the variation in the coefficient of friction as the contact conditions change.

$$\mu(\xi) = c_0 + c_1 \cdot F_n(\xi)^{c_2} \cdot v_g(\xi)^{c_3} \cdot R(\xi)^{c_4} \quad (10.54)$$

The following units should be used: normal load  $F_n$  (N), absolute sliding speed  $v_g$  (m/s), and the equivalent curvature radius  $R$  (mm).

The coefficients proposed by Takanashi and Xiong equations are summarized in Table 10.6. The coefficients  $c_0$  and  $c_1$  were adjusted for the two material pairings in this study. To achieve this, the coefficient of friction value from *VDI-2736 Blatt 2: Thermoplastic Gear Wheels - Cylindrical Gears-* (2013), as presented in Table 10.1, was used to adjust the equation average along the path of contact. This calibration was carried out exclusively for the theoretical path of contact, as the Takanashi equation exhibits a singularity when the load vanishes out of the theoretical path of contact. The coefficients proposed by Miller’s method were not included because the experiments were conducted using a polyoxymethylene (POM) material filled with polytetrafluoroethylene (PTFE).

Fig. 10.9 provides a visual comparison between the Takanashi and Xiong equations after applying the coefficients from Table 10.6. The Takanashi equation tends to yield smaller values near the pitch point but larger values near the mesh’s starting and ending points.

**Table 10.6** Original and modified coefficients for Takanashi (Takanashi & Shoji, 1981) and Xiong (Xiong & Zongshan, 2023) equations.

Author	Version	$c_0$	$c_1$	$c_2$	$c_3$	$c_4$
(Takanashi & Shoji, 1981)	Original	0.000	0.110	− 0.100	0.230	0.000
	Plastic/ plastic		0.168			
	Plastic/ steel		0.178			
(Xiong & Zongshan, 2023)	Original	0.081	0.330	0.312	0.251	− 0.375
	Plastic/ plastic	0.094	0.382			
	Plastic/ steel	0.103	0.420			

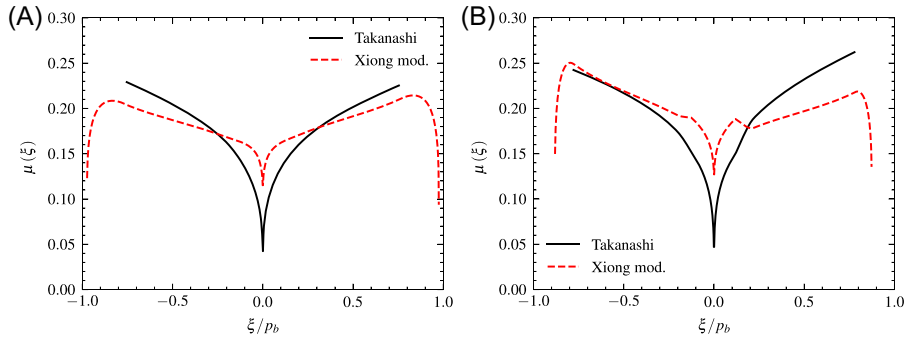


**Figure 10.9** Comparison of coefficient of friction equations.

## 10.5 Model implementation and verification against experiments

The model is implemented following the procedure described in the flowchart of Fig. 10.10. The model is initialized by setting the gear geometric parameters, the operating conditions, and the material elastic properties at the environment temperature ( $T_\infty$ ).

The analytical part of the model precedes the numerical one, enabling the calculation of essential parameters such as the heat transfer coefficients, the load-sharing ratio, the coefficient of friction, and the time-averaged frictional heat flux. The time-averaged frictional heat flux is shown in Fig. 10.11 for the considered gear pairings. The comparison between incorporating a local coefficient of friction and using a constant value along the contact path reveals noticeable differences mainly at the beginning and ending of the contact meshing process. The achieved results align with prior finite element solutions (Roda-Casanova & Sanchez-Marin, 2019).

The model has been designed to account for tooth temperature's influence on elastic properties. For cases where the bulk temperature closely matches the ambient temperature, a single iteration is sufficient, typically taking only a few seconds (depending on the mesh discretization) to run the analytical and numerical model. However, when the material's elastic properties change significantly with increasing bulk temperature, a different strategy should be considered. After the initial iteration, the temperature field is obtained and a volume-weighted average temperature ( $\bar{T}_{vol}$ ) is computed. The elastic properties for subsequent iterations are then based on this derived temperature.

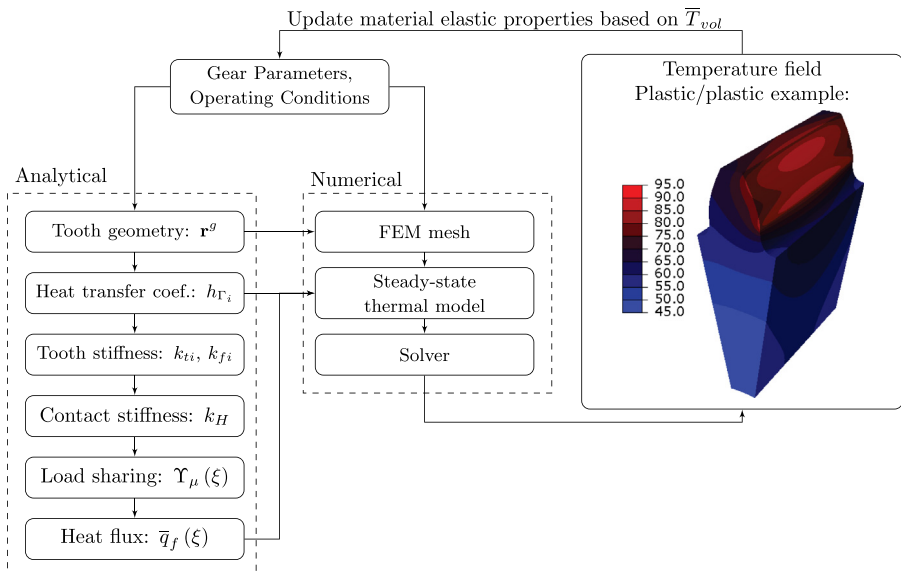


**Figure 10.10** Semi-analytical model implementation.

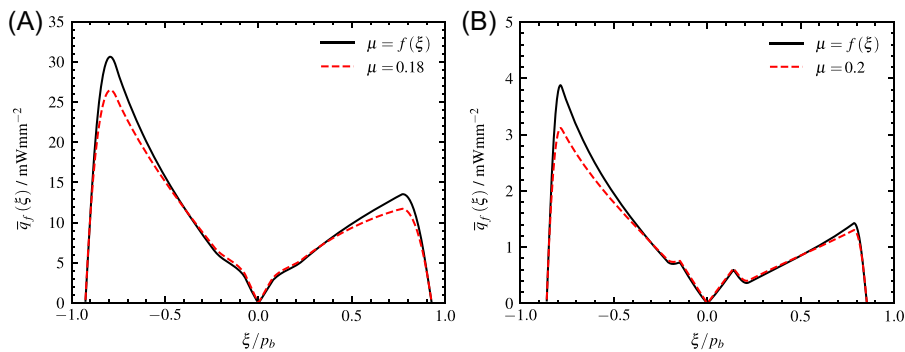


**Figure 10.11** Frictional heat flux. Time-averaged frictional heat flux.

**Table 10.7** Comparison of different convective models against experiments (values in °C).

Gear pairing	Pinion speed/rpm	Convective model	$T_{\min}$	$T_{\max}$	$\bar{T}_{vol}$	$\bar{T}_{\Gamma_M}$	$T_{exp}$
plastic/ plastic	823	Fernandes	46.4	80.2	57.3	73.9	65.0
		Černe	35.0	55.3	39.0	50.0	
		Roda-Casanova	45.5	72.7	53.3	67.4	
		Fernandes	51.3	113.5	70.3	101.3	
plastic/ steel	1646	Černe	40.1	80.2	48.0	70.0	89.0
		Roda-Casanova	46.2	95.2	70.3	84.8	
	600	Fernandes	32.4	43.7	35.3	41.0	44.5 ± 2.2
		Černe	31.3	39.7	32.7	37.0	
		Roda-Casanova	31.6	40.9	33.5	38.2	
	1200	Fernandes	31.0	41.5	33.5	38.8	46.3 ± 2.3
		Černe	30.6	38.8	31.9	36.2	
		Roda-Casanova	30.2	38.9	31.8	36.1	

The accuracy of the steady-state thermal finite element model presented was already validated with experiments as presented in a previous work (Fernandes et al., 2018). The various convective models discussed in this study were implemented because it was not possible to determine the most accurate one in advance. The Xiong equation with the coefficients from Table 10.6 was used to estimate the coefficient of friction. The finite element mesh was composed of 8-node linear isoparametric elements specifically designed for heat transfer problems (DC3D8), with 165,879 nodes for the plastic/plastic example and 745,281 nodes for the plastic/steel example.

The criterion for comparison with the available experiments was the average mesh flank temperature ( $\bar{T}_{\Gamma_M}$ ). Additionally, the minimum ( $T_{\min}$ ), maximum ( $T_{\max}$ ), and volume-weighted average ( $\bar{T}_{vol}$ ) temperatures are shown for reference. Based on the results obtained and presented in Table 10.7, it can be concluded that employing the Roda-Casanova convective model fairly aligns better with



experimental data if the trend of results is considered. A slight deviation between the experiments and the temperature predicted by the model is observed. A possible reason for the deviation is due to the omission of hysteresis losses in the model, which may be significant for polymer gears (Roda-Casanova & Fernandes, 2022). To overcome this limitation, one proposed solution is the incorporation of hysteresis losses along the meshing surface, as indicated in Roda-Casanova and Fernandes (2022). It is essential to note, however, that this introduces a simplification to the problem. To precisely capture the physics of hysteric losses in a steady-state thermal finite element model, further efforts are recommended. This is particularly crucial in the case of the plastic/steel example, which experiences a low frictional heat flux due to the very low heat partition factor and the predicted values consistently fall below the experimental data, irrespective of the convective model employed. Additionally, the existing models still present some uncertainty on the coefficient of friction prediction.

## 10.6 Outlook

The operating temperature is a critical factor in designing polymer gears due to its profound impact on their mechanical properties and strength. While various analytical models are frequently employed, they often come with inherent limitations. In contrast, a thermo-mechanical finite element analysis of the problem under consideration is sometimes unfeasible and resource-consuming. However, the steady-state thermal finite element model typically offers an accurate solution of the temperature field when compared to the available simplified analytical models while providing a low computational time cost and may be considered for gear optimization tasks. The primary limitation of using a finite element model to solve the thermo-mechanical problem lies in the tooth contact analysis required to accurately predict the frictional heat flux. The presented methodology overcomes this limitation without sacrificing accuracy by employing an analytical loaded tooth contact analysis.

The presented methodology allows a fast calculation of various crucial parameters related to polymer gear meshing such as load-sharing ratio, coefficient of friction, power loss, and frictional heat flux.

A typical simplification of the existing models to predict polymer gear operating temperature is to use a constant coefficient of friction value along the gear path of contact. A variable coefficient of friction along the path of contact was considered by using reference equations from the literature.

A required input for any polymer gear thermal model is the convective heat transfer coefficient. Several methodologies were presented and compared and the one originating from CFD calculations is observed to provide a better agreement with the experiments.

Overall, the presented methodology is useful for predicting the temperature field and also for obtaining relevant polymer gear meshing parameters during the optimization and design phases.

## References

- Argyris, J. H., Fuentes, A., & Litvin, F. L. (2002). Computerized integrated approach for design and stress analysis of spiral. *Computer Methods in Applied Mechanics and Engineering*, 191, 1057–1095. Available from [https://doi.org/10.1016/S0045-7825\(01\)00316-4](https://doi.org/10.1016/S0045-7825(01)00316-4).
- Blok, H. (1963). *The flash temperature concept*. *Wear*, 6, 483–494.
- Bowden, F. P., & Ridler, K. E. W. (1936). Thomas Martin Lowry, physical properties of surfaces - III—The surface temperature of sliding. *Proceedings of the Royal Society of London. Series A - Mathematical and*, 154(883), 640–656. Available from <https://doi.org/10.1098/rspa.1936.0074>.
- Çengel, Y.A. (2003). *Heat transfer: A practical approach*. McGraw-Hill series in mechanical engineering. McGraw-Hill.
- Černe, B., Petkovšek, M., Duhovnik, J., & Tavčar, J. (2020a). Thermo-mechanical modeling of polymer spur gears with experimental. *Mechanism and Machine Theory*, 146, 103734. Available from <https://doi.org/10.1016/j.mechmachtheory.2019.103734>.
- Cooley, C. G., Liu, C., Dai, X., & Parker, R. G. (2016). Gear tooth mesh stiffness: A comparison of calculation approaches. *Mechanism and Machine Theory*, 105, 540–553. Available from <https://doi.org/10.1016/j.mechmachtheory.2016.07.021>.
- Fernandes, C. M. C. G., Marques, P. M. T., Martins, R. C., & Seabra, J. H. O. (2015). Gearbox power loss. Part II: Friction losses in gears. *Tribology International*, 88, 309–316. Available from <https://doi.org/10.1016/j.triboint.2014.12.004>.
- Fernandes, C. M. C. G., Martins, R. C., & Seabra, J. H. O. (2014). Torque loss of type C40 FZG gears lubricated with wind turbine gear oils. *Tribology International*, 70, 83–93. Available from <https://doi.org/10.1016/j.triboint.2013.10.003>.
- Fernandes, C. M. C. G., Martins, R. C., & Seabra, J. H. O. (2016). Coefficient of friction equation for gears based on a modified Hersey. *Tribology International*, 101, 204–217. Available from <https://doi.org/10.1016/j.triboint.2016.03.028>.
- Fernandes, C. M. C. G., Rocha, D. M. P., Martins, R. C., Magalhaes, L., & Seabra, J. H. O. (2019). Hybrid polymer gear concepts to improve thermal behavior. *Journal of Tribology*, 141. Available from <https://doi.org/10.1115/1.4041461>.
- Fernandes, C. M. C. G., Rocha, D. M. P., Martins, R. C., Magalhães, L., & Seabra, J. H. O. (2018). Finite element method model to predict bulk and flash temperatures on. *Tribology International*, 120, 255–268. Available from <https://doi.org/10.1016/j.triboint.2017.12.027>.
- Gurskii, B. E., & Chichinadze, A. (2007). Frictional heat problem and its evolution. Part 1. Blok model and its. *Journal of Friction and Wear*, 28, 316–329. Available from <https://doi.org/10.3103/S1068366607030130>.
- Hachmann, H., & Strickle, E. (1966). Polyamide als Zahnradwerkstoffe. *Konstruktion*, 18(3), 81–94.
- Hall, K. W., & Alvord, H. H. (1956). Capacity of nylon plastic gears. *Machine Design*, 28(8), 120.
- Hartnett, J. P., & Deland, E. C. (1961). The influence of Prandtl number on the heat transfer from rotating. *Journal of Heat Transfer*, 83(1), 95. Available from <https://doi.org/10.1115/1.3680479>.
- Handschuh, R. F. (1993). Thermal behavior of spiral bevel gears. Case Western Reserve University.
- Holman, J.P.. (1986). *Heat transfer*. McGraw Hill.

- Hooton, J. D. S., Gonçalves, D. E. P., & Fernandes, C. M. C. G. (2023). Experiments and finite element analysis on a hybrid polymer gear rack. *Mechanism and Machine Theory*, 186, 105363. Available from <https://doi.org/10.1016/j.mechmachtheory.2023.105363>.
- Hsiang, L., Jifeng, W., Fred, O., & John, C. (1993). 29th Joint Propulsion Conference & Exhibit, 1993, Monterey, CA. Available as NASA Technical Memorandum 106/74. <https://www.geartechnology.com/ext/resources/issues/0794x/oswald.pd>.
- Kalin, M., & Kupec, A. (2017). The dominant effect of temperature on the fatigue behaviour of polymer. *Wear*, 376–377, 1339–1346. Available from <https://doi.org/10.1016/j.wear.2017.02.003>.
- Karimpour, M., Dearn, K. D., & Walton, D. (2010). A kinematic analysis of meshing polymer gear teeth. *Proceedings of the Institution of Mechanical Engineers, Part L: Journal of Materials: Design and Applications*, 224, 101–115. Available from <https://doi.org/10.1243/14644207JMDA315>.
- Knudsen, J. G., Katz, D. L., & Street, R. E. (1959). Fluid dynamics and heat transfer. *Physics Today*, 12(3), 40–44.
- Koffi, D., Gauvin, R., & Yelle, H. (1985). Heat generation in thermoplastic spur gears. *Journal of Mechanisms, Transmissions and Automation in Design*, 107, 31–36. Available from <https://doi.org/10.1115/1.3258688>.
- Letzelter, E., Vaujany, J.-P. de, Chazeau, L., & Guingand, M. (2009). Quasi-static load sharing model in the case of Nylon 6/6 cylindrical gears. *Materials & Design*, 30(10), 4360–4368. Available from <https://doi.org/10.1016/j.matdes.2009.04.008>.
- Li, W., Zhai, P., Tian, J., & Luo, B. (2018). Thermal analysis of helical gear transmission system considering machining. *International Journal of Mechanical Sciences*, 149, 1–17. Available from <https://doi.org/10.1016/j.ijmecsci.2018.09.036>.
- Litvin, F. L., Fuentes, A. Gear geometry and applied theory. Cambridge University Press, (2004).
- Lu, Z., Liu, H., Wei, P., Zhu, C., Xin, D., & Shen, Y. (2020). The effect of injection molding lunker defect on the durability. *International Journal of Mechanical Sciences*, 180, 105665. Available from <https://doi.org/10.1016/j.ijmecsci.2020.105665>.
- Luo, B., & Li, W. (2016). Influence factors on bulk temperature field of gear. *Proceedings of the Institution of Mechanical Engineers, Part J: Journal of Engineering Tribology*. Available from <https://doi.org/10.1177/1350650116684275>.
- Maag Gear Company Ltd. (1990). *Maag gear book: Calculation and practice of gears, gear drives toothed*. Maag Gear Company Limited.
- Mao, K. (1993). The performance of dry running non-metallic gears. PhD thesis, University of Birmingham.
- Mao, K. (2007). A numerical method for polymer composite gear flash temperature prediction. *Wear*, 262, 1321–1329. Available from <https://doi.org/10.1016/j.wear.2007.01.008>.
- Mao, K., Li, W., Hooke, C. J., & Walton, D. (2010). Polymer gear surface thermal wear and its performance prediction. *Tribology International*, 43(1), 433–439. Available from <https://doi.org/10.1016/j.triboint.2009.07.006>.
- Marafona, J. D. M., Marques, P. M. T., Martins, R. C., & Seabra, J. H. O. (2021). Mesh stiffness models for cylindrical gears: A detailed review. *Mechanism and Machine Theory*, 166. Available from <https://doi.org/10.1016/j.mechmachtheory.2021.104472>.
- Marafona, J. D. M., Marques, P. M. T., Portron, S., Martins, R. C., & Seabra, J. H. O. (2023). Gear mesh stiffness and dynamics: Influence of tooth pair structural. *Mechanism and Machine Theory*, 190, 105447. Available from <https://doi.org/10.1016/j.mechmachtheory.2023.105447>.

- Marques, P. M. T., Marafona, J. D. M., Martins, R. C., & Seabra, J. H. O. (2021). A continuous analytical solution for the load sharing and friction torque. *Mechanism and Machine Theory*, 161, 104320. Available from <https://doi.org/10.1016/j.mechmachtheory.2021.104320>.
- Miler, D., Hoi, M., Domitran, Z., & Žeželj, D. (2019). Prediction of friction coefficient in dry-lubricated polyoxymethylene spur. *Mechanism and Machine Theory*, 138, 205–222. Available from <https://doi.org/10.1016/j.mechmachtheory.2019.03.040>.
- Miler, D., & Hoić, M. (2021). Optimisation of cylindrical gear pairs: A review. *Mechanism and Machine Theory*, 156, 104156. Available from <https://doi.org/10.1016/j.mechmachtheory.2020.104156>.
- Miler, D., Hoić, M., Škec, S., & Žeželj, D. (2020). Optimisation of polymer spur gear pairs with experimental validation. *Structural and Multidisciplinary Optimization*, 62, 3271–3285. Available from <https://doi.org/10.1007/s00158-020-02686-1>.
- Millsaps, K., & Pohlhausen, K. (1952). Heat transfer by laminar flow from a rotating plate. *Journal of the Aeronautical Sciences*, 19(2), 120–126. Available from <https://doi.org/10.2514/8.2175>.
- Munro, R. G., Morrish, L., & Palmer, D. (1999). Gear transmission error outside the normal path of contact due to corner. *Proceedings of the Institution of Mechanical Engineers, Part C: Journal of*, 213(4), 389–400. Available from <https://doi.org/10.1243/0954406991522347>.
- Patir, N., & Cheng, H. S. (1979). Prediction of the bulk temperature in spur gears based on finite element. *A S L E Transactions*, 22(1), 25–36. Available from <https://doi.org/10.1080/05698197908982899>.
- Pedrero, J. I., Pleguezuelos, M., Artés, M., & Antona, J. A. (2010). Load distribution model along the line of contact for involute external. *Mechanism and Machine Theory*, 45(5), 780–794. Available from <https://doi.org/10.1016/j.mechmachtheory.2009.12.009>.
- Pogacnik, A., & Tavcar, J. (2015). *VDI Gear Conference 2015, Munich, Accelerated testing method for polymer gears Review of gear body temperature calculation according to VDI 2736*.
- Reimann, T., Herzog, T., Kadach, D., & Stahl, K. (2019). The influence of friction on the tooth normal force of spur and helical. *Proceedings of the Institution of Mechanical Engineers, Part C: Journal of*. 233 (21–22), 7391–7400. Available from <https://doi.org/10.1177/0954406219855097>.
- Roda-Casanova, V., & Fernandes, C. M. C. G. (2022). A comparison of analytical methods to predict the bulk temperature in. *Mechanism and Machine Theory*, 173, 104849. Available from <https://doi.org/10.1016/j.mechmachtheory.2022.104849>.
- Roda-Casanova, V., & Sanchez-Marin, F. (2019). A 2D finite element based approach to predict the temperature field. *Mechanism and Machine Theory*, 133, 195–210. Available from <https://doi.org/10.1016/j.mechmachtheory.2018.11.019>.
- Roda-Casanova, V., Sanchez-Marin, F., & Martinez-Cuenca, R. (2023). Convective heat transfer modelling in dry-running polymer spur gears. *International Journal of Mechanical Sciences*, 0020–7403, 241. Available from <https://doi.org/10.1016/j.ijmecsci.2022.107927>.
- Sainsot, P., & Velez, P. (2020). On contact deflection and stiffness in spur and helical gears. *Elsevier Ltd, France Mechanism and Machine Theory*, 154. Available from <https://doi.org/10.1016/j.mechmachtheory.2020.104049>, <https://www.journals.elsevier.com/mechanism-and-machine-theory>.
- Sainsot, P., Velez, P., & Duverger, O. (2004). Contribution of gear body to tooth deflections—A new bidimensional. *Journal of Mechanical Design*, 126(4), 748–752.

- Shunlei, Y. (2010). The simulation analysis of transient temperature of spiral bevel gear. *Technologies & Products*, 43–48.
- Singh, A., & Houser, D. R. (1994). Analysis of off-line of action contact at the tips of gear teeth. *SAE Transactions*, 103, 196–203.
- Singh, P. K., Siddhartha., & Singh, A. K. (2018). An investigation on the thermal and wear behavior of polymer based spur. *Tribology International*, 118, 264–272. Available from <https://doi.org/10.1016/j.triboint.2017.10.007>.
- Takanashi, S., & Shoji, A. (1979a). Über den Temperaturanstieg von Zähnen von Kunststoffzahnradern, 2. Science reports of the Research Institutes. *Tohoku University. Ser. A*, 28, 103–115.
- Takanashi, S., & Shoji, A. (1979b). Über den Temperaturanstieg von Zähnen von Kunststoffzahnradern, 1. Science reports of the Research Institutes. *Tohoku University. Ser. A*, 28, 93–102.
- Takanashi, S., & Shoji, A. (1981). Measurement of the coefficient of kinetic friction of plastic materials. *Journal of the Japan Society of Precision Engineering*, 47(8), 944–948. Available from <https://doi.org/10.2493/jjspe.1933.47.944>.
- Tavčar, J., Cerne, B., Duhovnik, J., & Zorko, D. (2021). A multicriteria function for polymer gear design optimization. *Journal of Computational Design and Engineering*, 8, 581–599. Available from <https://doi.org/10.1093/jcde/qwaa097>.
- Terashima, K., Tsukamoto, N., Nishida, N., & Shi, J. (1986). Development of plastic gears for power transmission. *Bulletin of JSME*, 29.
- Timoshenko, S., & Baud, R. V. (1926). Strength of gear teeth is greatly affected by fillet radius. *Automotive Industries*, 55, 138–142.
- Tsukamoto, N., & Terashima, K. (1985). Development of plastic gears for power transmission. *Various Methods of Transactions of the Japan Society of Mechanical Engineers Series C*, 51, 1107–1112. Available from <https://doi.org/10.1299/kikaic.51.1107>.
- Takanashi, S. & Shoji, A. (1980). Third ASME International power transmission and gearing conference (San Francisco, August 1980).
- VDI -2736. (2014). Thermoplastic Gear Wheels – Calculation of the Load-Carrying Capacity. Part 2. Verein Deutscher Ingenieure, Düsseldorf.
- Walton, D., & Shi, Y. W. W. (1989). A comparison of ratings for plastic gears. *Proceedings of the Institution of Mechanical Engineers, Part C: Journal of Mechanical Engineering Science*, 203, 31–33. Available from [https://doi.org/10.1243/PIME\\_PROC\\_1989\\_203\\_083\\_02](https://doi.org/10.1243/PIME_PROC_1989_203_083_02).
- Wang, K. L., Cheng, H. S. (1980). Thermal elastohydrodynamic lubrication of Spur Gears.
- Weber, C., & Banaschek, K. (1953). *Formänderung und Profilrücknahme bei Gerad- und Schrägverzahnungen*. F. Vieweg und Sohn.
- Xiong, K. H. Y., & Zongshan, Z. (2023). Study on friction characteristics of ADC12-POM gear pair. *Tribology Transactions*, 66(4), 771–785. Available from <https://doi.org/10.1080/10402004.2023.2234415>.
- Yelle, H., & Burns, D. J. (1981). Calculation of contact ratios for plastic/plastic or plastic/steel spur. *Journal of Mechanical Design*, 103(2).
- Zhiliang, X., Wennian, Y., & Yimin, S. (2021). A refined analytical model for the mesh stiffness calculation of plastic. *Applied Mathematical Modelling*, 98, 71–89. Available from <https://doi.org/10.1016/j.apm.2021.04.032>.
- Zorko, D., Kulovec, S., Duhovnik, J., & Tavčar, J. (2019). Durability and design parameters of a Steel/PEEK gear pair. *Mechanism and Machine Theory*, 140, 825–846. Available from <https://doi.org/10.1016/j.mechmachtheory.2019.07.001>.